Role of Co Content on the Electrode Properties of P3-Type $K_{0.5}Mn_{1-x}Co_xO_2$ Potassium Insertion Materials

Pawan Kumar Jha and Prabeer Barpanda*

ABSTRACT: Potassium-ion batteries are widely being pursued as potential candidates for stationary (grid) storage, where energy dense K^+ insertion cathodes are central to economic and energy efficient operation. To develop robust K-based cathodes, it is key to correlate their underlying electronic states to the final electrochemical performance. Here, we report the synthesis and structure−electrochemical property correlation in P3-type $K_{0.5}Mn_{1-x}Co_xO_2$ binary layered oxide cathodes. Spectroscopic analyses revealed a random distribution of Mn and Co in transition metal layers in the oxygen anion framework. In this solid-solution family, Co substitution improved the electronic conductivity and structural stability of P3 phases by minimizing local lattice distortion. Co substitution led to a systematic shift of the Co^{4+}/Co^{3+} and Mn^{4+}/Mn^{3+} redox potentials. Galvanostatic cycling showed that the Co substitution reduced the initial capacity while improving the cycling stability. The role of Co on final electrochemical properties of P3-layered oxides has been elucidated as a design tool to develop practical potassium-ion batteries.

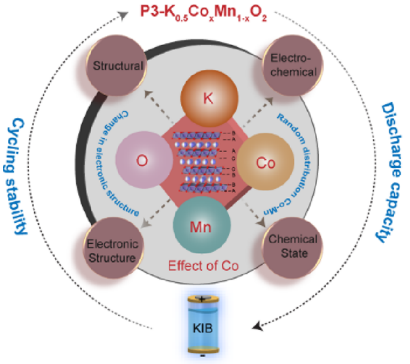

1. INTRODUCTION

Over the last three decades, there has been a steady growth in the industrial demand for energy storage devices targeting applications including consumer electronics to electric vehicles.[1,2] Secondary K-ion batteries (KIBs) form a pragmatic energy storage systems beyond the state-of-the-art Li-ion batteries (LIBs), particularly suitable for stationary storage.[3,4] Electrochemical cells based on mobile carrier K^+ are projected to provide efficient energy storage because of comparative ionic diffusion in bulk, weak Lewis's acidity allowing easy desolvation, and faster interfacial charge transfer. Additionally, a weaker K^+ ion−solvent interaction can promote fast K^+ diffusion and high conductivity in electrolytes. Importantly, a lower K^+/K standard electrode potential (E^0) than that of Li^+/Li in ester solvents like propylene carbonate (PC) (−0.09 V vs Li^+/Li) and ethylene carbonate (EC):diethyl carbonate (DEC) (−0.12 V vs Li^+/Li) allows KIBs to operate at high potential with a comparable energy density.[5] Furthermore, a more negative potential E^0 suggests a lower-potential limitation in choosing negative electrodes for KIBs over LIBs.[3] Despite these merits, the practical implementation of KIB is hindered by the lack of suitable cathodes capable of reversible K^+ (de)insertion at optimum voltage delivering high capacity, swift rate, and prolonged cycle life.

Based on the intercalation chemistry, most of the KIB cathode materials are similar to those studied for LIBs and NIBs (Na-ion batteries). The ideal host can accommodate enough mobile guest K^+ ions without irreversible phase transitions. Here, layered oxide materials have interesting chemical and physical properties capable of reversible K^+ (de) insertion. Thus, a suite of layered oxides have been studied as potential cathodes for KIBs. Especially, P3-type oxides have gained tremendous attention owing to their two-dimensional layered structures, offering fast K^+ migration and high energy density.[6−9] In P3-layered structures, a large K^+ ion strongly stabilizes the layered structure by occupying the prismatic site between $[MO_2]_n$ layers. The structural stability of P3-K_xMO_2 can be explained through the correlation between the ionic radii of the alkali (R_{A+}) and transition ($R_{M3+/M4+}$) metals.[10,11] The larger ionic size of K^+ favors P3-type layered transition metal oxides that can be easily prepared by a conventional solid-state route. Among various P3 phases, K_xMnO_2 can intercalate a considerable amount of K^+ (per f.u.) due to its superior structural flexibility.[12,13] For charge compensation in the K^+-deficient K_xMnO_2 layered oxides, Mn exists in mixed oxidation states (i.e., x number of Mn has 3+ oxidation state and $(1-x)$ number of Mn has 4+ oxidation state). The presence of Jahn−Teller active high-spin Mn^{3+} ($3d^4$) ions not only increases the effective activation barrier for cation diffusion, but also destabilizes the structure by introducing stacking faults and other defects leading to irreversible phase transition at high voltage or low K^+ content.[13] Literature indicates partial substitution of Mn with other transition metal ions and/or redox inactive cations can increase the amount of

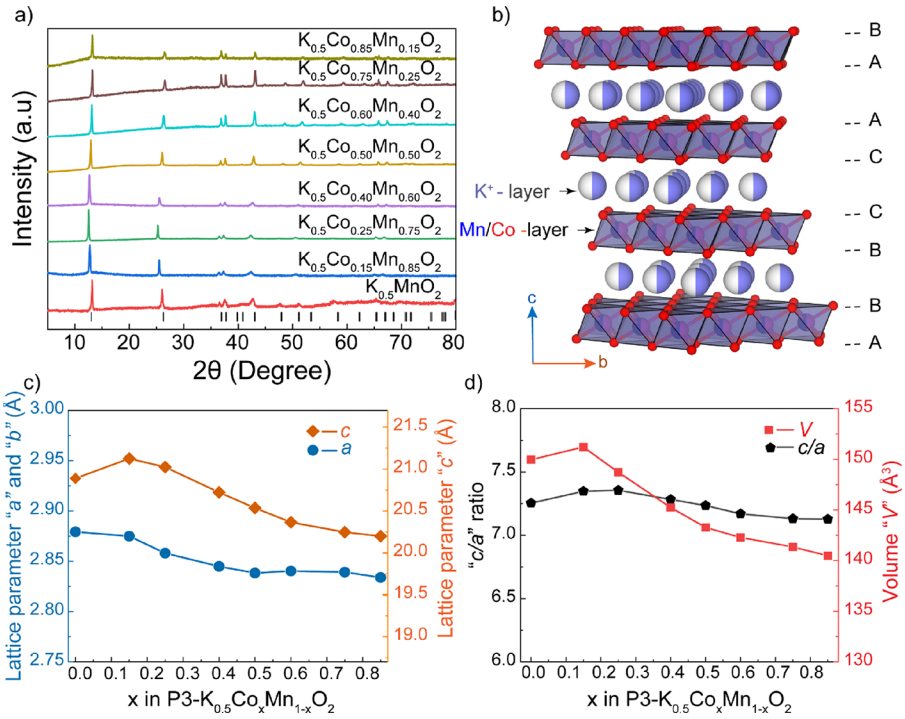

Figure 1. (a) Powder X-ray diffraction patterns of P3-type $K_{0.5}Mn_{1-x}Co_xO_2$ insertion compounds. The simulated pattern for the reference P3-type $K_xCo_{0.6}Mn_{0.4}O_2$ is shown for comparison.[20] Bragg diffraction peaks are shown by black vertical ticks. (b) Illustration of P3-type $K_{0.5}MM'O_2$ (M and M′ = transition metals) layered oxide structure representing the ABBCCA oxygen anions layer stacking. (c, d) Variation of unit cell parameters as a function of x in P3-type $K_{0.5}Mn_{1-x}Co_xO_2$ materials. The lines are provided as guides for the eye.

Mn^{4+} ions in the layered structure that can circumvent undesirable structural instability and phase transformation.[6,8,14] Thus, such systems can outperform the parent K_xMnO_2 in terms of capacity retention and rate kinetics due to the diminished detrimental effect associated with Mn^{3+} ions.

In particular, Co substitution in manganese (Mn)-based layered oxides is expected to exhibit a synergistic impact by combining the high capacity of Mn redox with the elevated redox voltage associated with Co redox. This dual enhancement strategy aims to improve electrode performance by augmenting both the electronic conductivity and K^+ ion conduction while concurrently addressing concerns related to Jahn−Teller structural instability.[6,8,15−17] Despite these promising attributes, it is essential to acknowledge that the use of cobalt is constrained by its toxicity, limited availability of resources, and hence high cost. For example, $K_{0.54}Mn_{0.5}Co_{0.5}O_2$ exhibited smooth (dis)charge curves, indicating a lower degree of J−T distortion in the host layered structure and K^+/vacancy ordering in the disordered Mn−Co binary phase.[18] It showed a fast rate capability with a solid-solution (de)potassiation reaction. In contrast, P3- $K_{0.45}Co_{0.5}Mn_{0.5}O_2$ exhibited sluggish K^+ migration and lower capacity undergoing a two-phase redox reaction.[19] Despite a high voltage with more Co doping in P3-$K_{0.48}Co_{0.6}Mn_{0.4}O_2$, it could only (de)intercalate 0.25 K^+ per formula unit in the broad potential window.[20] Although K^+ ordering or oxide layer gliding may cause structural transformations accompanying the (dis)charge process, the relationship between the electronic state and electrochemical characteristics has not yet been fully elucidated. It calls for a detailed study of the structural, electronic, and electrochemical properties to understand and optimize the P3-type $K_{0.5}Mn_{1-x}Co_xO_2$ cathode for future application.

In the current work, we focus on a series of P3-layered $K_{0.5}Mn_{1-x}Co_xO_2$ ($0 < x < 0.85$) oxides. These compounds were synthesized via a soft chemistry-based solution combustion route and were probed as KIB cathode materials. By using spectroscopic techniques (FTIR and Raman), we have investigated the local structure of these compounds. We noticed that cobalt substitution for Mn is an easy way to stabilize a two-dimensional (2D) layer structure. Furthermore, capacity loss and structural integrity are markedly enhanced upon cycling for Co-substituted transition metal oxides. Importantly, we observed that substituting Co in place of Mn led to a systematic shift in the potentials of the Co^{4+}/Co^{3+} and Mn^{4+}/Mn^{3+} redox couples. The Co^{4+}/Co^{3+} redox couple shifted to a lower potential, while the Mn^{4+}/Mn^{3+} redox couple shifted to a higher potential. This is due to the inductive effect of Co on Mn, which results in a delocalization of electrons away from the Mn atoms. This systematic study provides guidelines for the compositional engineering of P3-type layered oxides to achieve stable and reversible K^+ (de)insertion activity.

2. MATERIALS AND METHODS

2.1. Material Synthesis. P3-type $K_{0.5}Mn_{1-x}Co_xO_2$ ($0 \le x < 1$) layered oxide compounds were synthesized via solution combustion synthesis (SCS). The synthesis scheme is depicted in Figure S1. Stoichiometric amounts of KNO_3 (SDFCL, 99%), $Mn(NO_3)_2{\cdot}4H_2O$ (Thermo Fisher Scientific, 98%), and $Co(NO_3)_2{\cdot}6H_2O$ (SDFCL, 99.5%) nitrate salts were dissolved in distilled water to yield the K, Mn, and Co molar ratio of 0.5:x:1−x. In addition to these nitrate oxidizers, citric acid ($C_6H_8O_7$, SDFCL, 99.5%) was added as a fuel to initiate citrate−nitrate gel formation. In addition, 5 wt % of excess KNO_3 was added to compensate for the inevitable K loss during the subsequent high-temperature annealing process. The resulting solution was heated to 120 °C to drive out the excess water.

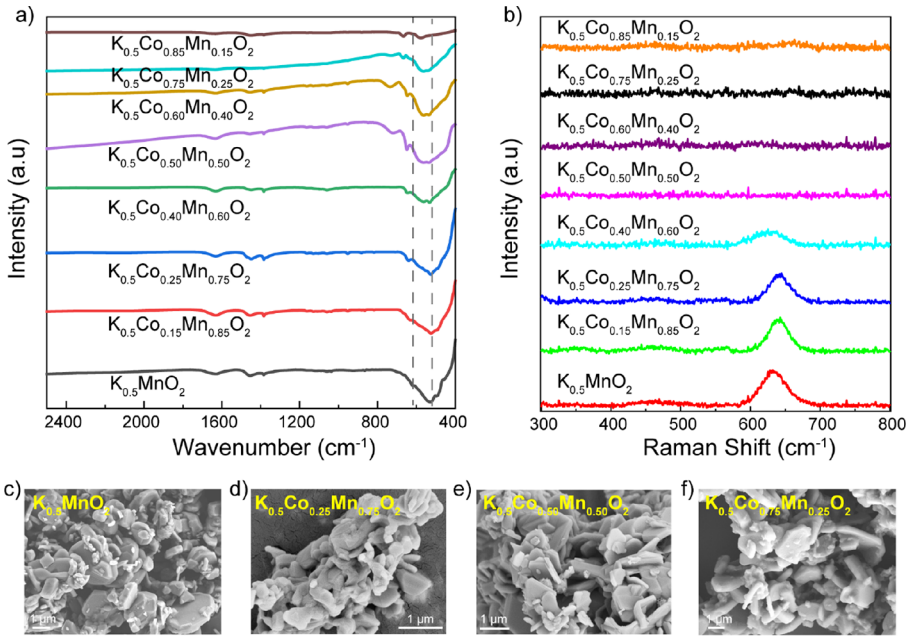

Figure 2. (a) Fourier transform infrared (FTIR) and (b) Raman scattering spectra of the P3-type $K_{0.5}Mn_{1-x}Co_xO_2$ family of materials. Representative SEM micrographs of (c) P3-$K_{0.5}MnO_2$, (d) P3- $K_{0.5}Co_{0.25}Mn_{0.75}O_2$, (e) P3-$K_{0.5}Co_{0.5}Mn_{0.5}O_2$, and (f) P3-$K_{0.5}Co_{0.75}Mn_{0.25}O_2$ composed of micrometric particle morphology irrespective of the Co content.

Following, the temperature was increased to 200 °C, where the thick reddish precursor solution rapidly transformed into a fluffy black intermediate complex. The obtained powder was mildly ground and annealed at 800 °C for 12 h in a muffle furnace to yield the desired P3-type $K_{0.5}Mn_{1-x}Co_xO_2$ oxide products. The net reaction can be expressed as follows:

$$0.5KNO_{3(s)} + xCo(NO_3)_2{\cdot}6H_2O_{(s)} + (1-x)Mn(NO_3)_2{\cdot}4H_2O_{(s)} + C_6H_8O_{7(s)} \rightarrow K_{0.5}Mn_{1-x}Co_xO_{2(s)} + NO_{y(g)}\uparrow + CO_{y(g)}\uparrow + H_2O_{(g)}\uparrow$$

2.2. Structural and Physical Characterization. The structural characterization was performed by powder X-ray diffraction (XRD) with a PANalytical X'Pert PRO MPD X-ray diffractometer in the 2θ range of 5−90° using the Cu Kα (λ = 1.5406 Å) source operating at 40 kV/30 mA. Rietveld analysis was carried out using FullProof software, and the layered structure was visualized using VESTA software.[21,22] Morphology was captured using scanning electron microscopy (Ultra 55 FESEM Carl Zeiss EDS, operated at 5−20 kV). The Fourier transform infrared (FTIR) spectra were acquired with a PerkinElmer (Frontier) instrument, and Raman spectra were recorded with a LabRAM HR unit (Horiba Jobin Yvon) equipped with a 532 nm (green) laser source. To gauge the oxidation state, X-ray photoelectron spectra (XPS) were taken with a Thermo Scientific K_α XPS instrument operating at 12 kV/6 mA. For XPS analyses, the samples were carefully transferred from the Ar-filled glovebox to the XPS chamber without any air exposure.

2.3. Electrochemical Measurements. For the electrochemical studies, electrode sheets were prepared by intimately mixing the as-synthesized $K_{0.5}Mn_{1-x}Co_xO_2$ active material, ketjen black (KB), and teflonized acetylene black (TAB) binder in the ratio of 70:20:10, respectively. These electrode sheets were used as the working electrode in assembly of CR2032 coin (half) cells along with potassium metal foil (acting as both reference and counter electrodes) separated by a sheet of glass fiber separator (Whatman, GF/C). This separator was soaked with 0.5 M KTFSI (bis-(trifluoromethanesulfonyl) imide) salt in Pyr_{13}TFSI in (1-methyl-1-propylpyrrolidinium bis(trifluoromethanesulfonyl) amide) acting as electrolyte. The details of this in-house prepared electrolyte is provided elsewhere.[23] All-cell assembly was performed inside an Ar-filled glovebox (MBRAUN LABStar GmbH, O_2 and H_2O < 0.5 ppm) to avoid any air/moisture contamination. The electrochemical testing was performed using the Neware BTS4000 battery tester in the potential window of 1.5−4.0 V (vs K/K^+) at a constant rate of C/20 at 25 °C. To derive the average voltage, three cells were subjected to electrochemical testing and their average values were taken.

3. RESULTS AND DISCUSSION

3.1. Crystal Structure and Morphological Analysis. The energy-savvy solution combustion method was successfully employed to synthesize the P3-type $K_{0.5}Mn_{1-x}Co_xO_2$ family of compounds. Figure 1a compares the XRD patterns of resulting products and reference patterns of P3-type $K_xCo_{0.6}Mn_{0.4}O_2$. Additionally, Figure S2 and Table S1 illustrate the Rietveld refinement results for $K_{0.5}Co_xMn_{1-x}O_2$ while Table S2 provides the occupancy values of the respective constituent elements. The intense peaks in each pattern could be indexed to a rhombohedral structure with a space group of *R*3*m* (#160) assuming the P3 phase with ABBCCA oxygen stacking. In addition, cooperative distortion was clearly evident by the broad XRD peaks for the Co-free and low Co content $K_{0.5}Mn_{1-x}Co_xO_2$ compounds (Table S3). The structural framework can be described as alternate MO_2 (M = transition metals) slabs of edge shared MO_6 octahedra and KO_6 triangular prisms sandwiched in the interlayer spacing along the [111] direction (Figure 1b). These MO_2 layers consist of randomly distributed Co and Mn due to the similar ionic radii of Co^{3+} (0.545 Å), Co^{4+} (0.53 Å), Mn^{3+} (0.645 Å), and Mn^{4+} (0.53 Å).[24] The six coordinated K^+ in a prismatic geometry share an edge on one side and face on the other side with MO_6 octahedra along the *c*-axis (Figure 1b). At *K* = 0.5, half of the potassium sites are occupied by K^+, where the potassium-ion occupancy in the prismatic sites strongly depends on the K content, the interaction between $K^+ - M^{3+/4+}$ (M= Mn, Co) and in-plane $K^+ - K^+$ electrostatic repulsion.

As shown in Figure 1c, the unit cell parameter *a* decreases from 2.879(8) to 2.845(6) Å with Co substitution up to 40%. It is due to the replacement of Jahn−Teller active Mn^{3+} ions by low-spin Co^{3+} ions. The ionic radii of Co^{4+} (0.53 Å) and Mn^{4+}

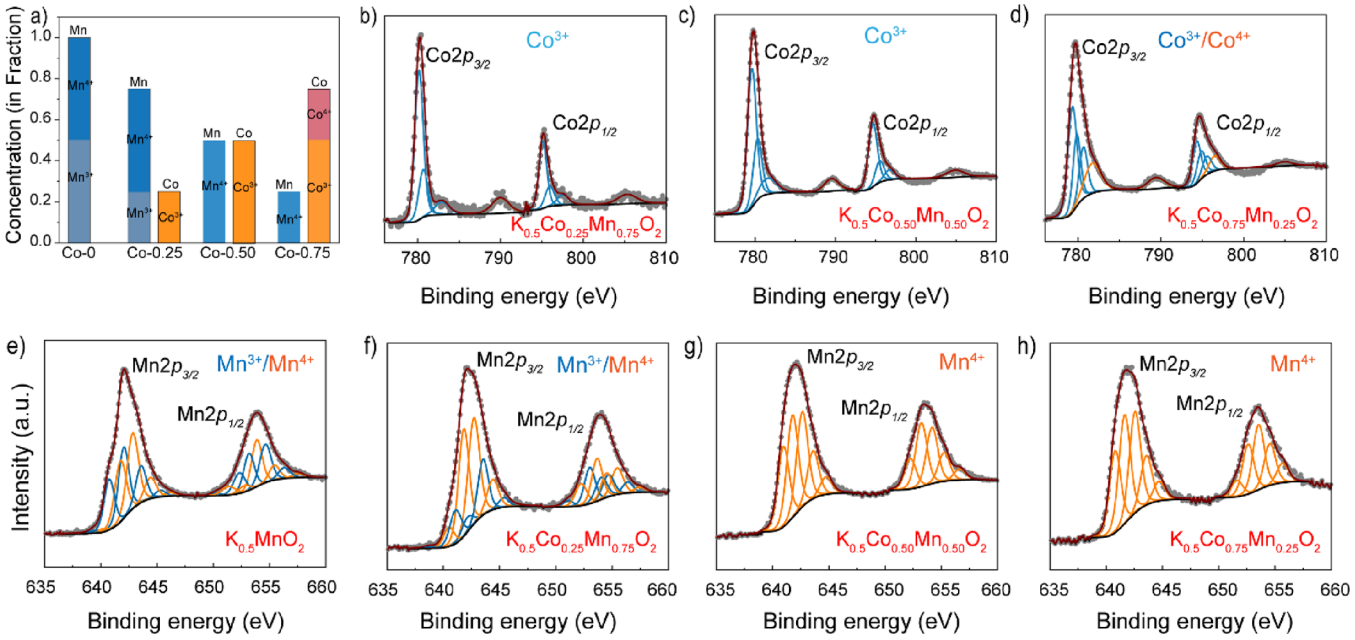

Figure 3. XPS spectra of P3-type $K_{0.5}Mn_{1-x}Co_xO_2$. (a) Summary of the relative amount of oxidation states of Mn and Co for different Co content. (b–d) Co 2*p* spectra for $x = 0.25$, $x = 0.5$, and $x = 0.75$ respectively. (e–h) Mn 2*p* spectra for $x = 0$, $x = 0.25$, $x = 0.5$, and $x = 0.75$, respectively. The blue curves and orange curves correspond to 3+ and +4 oxidation states.

(0.53 Å) are nearly identical, so the unit cell parameter does not change significantly as the Co content increases beyond 40%. The lattice parameter *c* first increases followed by a steady decrease with Co incorporation. The higher *c* value for higher Mn concentration can be explained by the larger ionicity of Mn–O bonds. This is due to the higher electronegativity difference between Mn and O atoms when compared to Co and O atoms. The larger ionicity of Mn–O bonds leads to a greater accumulation of negative charge on oxygen ions, which in turn develops more steric repulsion between the MO_2 layers. The anisotropic variation of the cell parameters in P3-$K_{0.5}Mn_{1-x}Co_xO_2$ is a complex phenomenon caused by the replacement of low-spin Co^{3+} ions with anisotropic Jahn–Teller Mn^{3+} ions and the oxygen uptake in the lattice.[17] The Jahn–Teller elongation axis is confined within the MO_2 layers, which causes the intralayer metal–metal distance to expand.

On the other hand, the interlayer metal–metal distance remains unaltered. This difference in the expansion of the intralayer and interlayer metal–metal distances leads to the anisotropic evolution of the cell parameters. In addition to replacing Co^{3+} with Mn^{3+}, the aliovalent replacement of Co^{3+} with Mn^{4+} accompanied by oxygen uptake can also affect the change in the unit cell parameters. The oxidation states of the transition metals and their bonding with neighboring oxygen anions can also alter the unit cell parameters. The unit cell volume ($V/Å^3$) of the P3-type $K_{0.5}Mn_{1-x}Co_xO_2$ ($0 \le x \le 0.85$) compounds demonstrates an initial increase with a low Co concentration (Figure 1d), followed by a decrease as the Co content rises. This observation confirms the successful formation of solid solutions of Mn and Co at transition metal (M) sites.

Afterward, the local structure of P3-type $K_{0.5}Mn_{1-x}Co_xO_2$ was investigated by FTIR and Raman scattering (RS) spectroscopy (Figure 2). These two vibrational spectroscopies are sensitive to the short-range environment of oxygen coordination around the cations in the oxide lattice. The band frequencies and relative intensities can shed light on the coordination geometry and electronic states. The primary FTIR spectrum of $K_{0.5}MnO_2$ contains absorption bands at 492, 533, and 624 cm^{-1}. These bands are in accordance with the spectrum observed for the M–O band presented in a similar kind of layered oxides and other M oxides.[25,26] While the first three lower-frequency bands stem from the characteristic vibrations of the M–O vibration bands, the subsequent three higher-frequency bands are associated with the characteristic vibrations of carbonate bands, which likely persist without undergoing reaction during the material synthesis. Due to the instrument limitation, we could not record the first band corresponding to the KO_6 polyhedra. As evident from Figure 2a, the shift of vibrational bands with the increase in the Co content confirms the formation of mixed Mn–Co layers in the lattice. The frequency shift of the stretching mode of the MO_2 octahedra can be attributed to the random distribution of Co and Mn in the MO_2 layers.

XRD and FTIR spectroscopy results show that replacing Mn with Co does not change the space group of P3-type $K_{0.5}Mn_{1-x}Co_xO_2$. However, Raman active bands in *R*3*m* symmetry were found to broaden and become less intense with increasing Co content (Figure 2b). It is due to a decrease in Jahn–Teller active Mn^{3+} ions, which in turn results in a reduction of the rhombohedral distortion by increasing Co content and/or an increase in the electrical conductivity in P3-type $K_{0.5}Mn_{1-x}Co_xO_2$ phases.[27,28] Also, higher Co substitution in $K_{0.5}Mn_{1-x}Co_xO_2$ was found to shift the Raman bands toward higher frequencies. In parallel, a high Co content reduces the unit cell parameters, e.g., the intralayer metal–metal distance (lattice parameter *a*) decreases from 2.879(8) to 2.834(4) Å. In simpler terms, the replacement of Co with Mn in P3- $K_{0.5}Mn_{1-x}Co_xO_2$ reduces the rhombohedral lattice distortion and enhances the electrical conductivity.[29,30] It results in the broadening and lower intensity of Raman active bands along with their shift to higher frequencies.

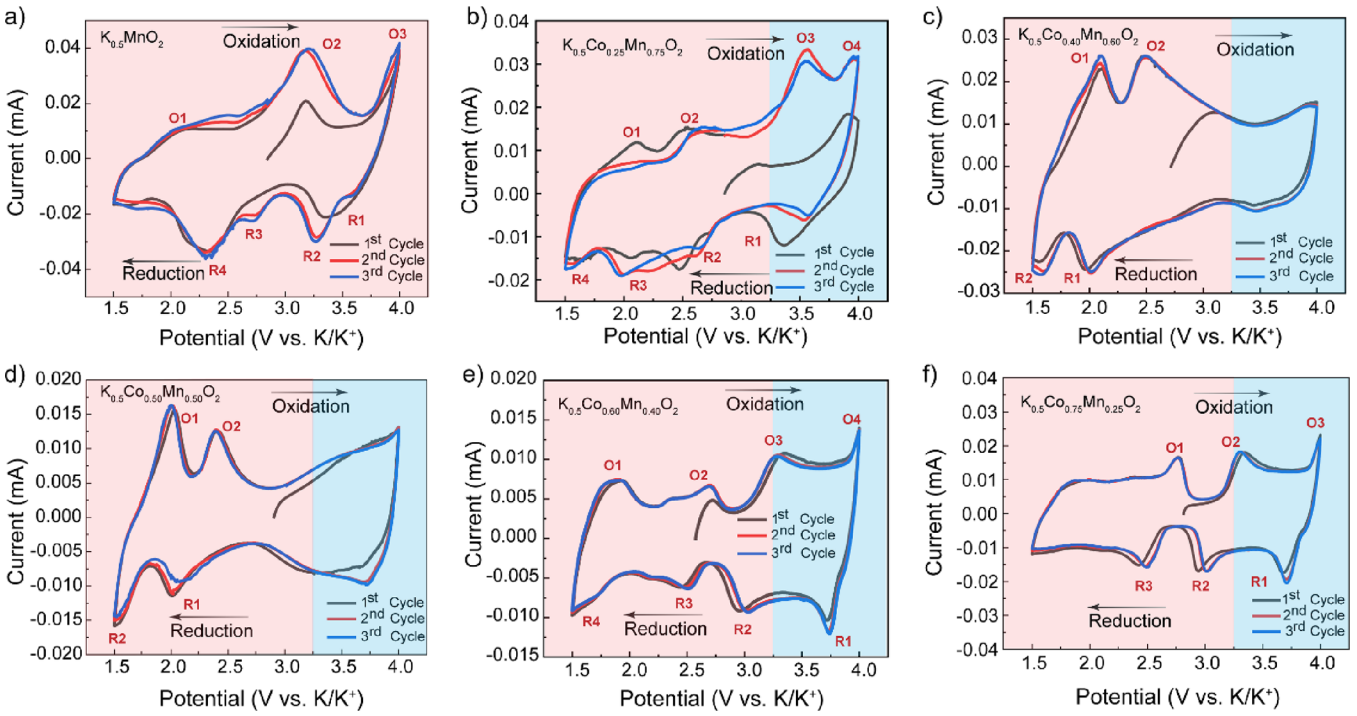

Figure 4. Cyclic voltammograms (vs K/K^+) of P3-type (a) $K_{0.5}MnO_2$, (b) $K_{0.5}Co_{0.25}Mn_{0.75}O_2$, (c) $K_{0.5}Co_{0.40}Mn_{0.60}O_2$, (d) $K_{0.5}Co_{0.5}Mn_{0.5}O_2$, (e) $K_{0.5}Co_{0.60}Mn_{0.40}O_2$, and (f) $K_{0.5}Co_{0.75}Mn_{0.24}O_2$ insertion materials at a scan rate of 0.05 mV s^{-1} in the potential window of 1.5–4.0 V.

The as-synthesized $K_{0.5}Mn_{1-x}Co_xO_2$ materials had hexagonal platelet-like morphology with micrometric particles (2–3 μm) (Figure 2c–f). The overall composition of these compounds was found to be closer to the nominal stoichiometry of phases along with uniform distribution of all constituent elements (K, Co, Mn, and O) as observed by energy dispersive (EDS) elemental analysis (Table S4 and Figure S3).

The chemical states of constituent elements in the $K_{0.5}Mn_{1-x}Co_xO_2$ phases were probed using XPS spectroscopy. Survey spectra (Figure S4) show representative peaks corresponding to K, Co, Mn, and O species. Co 2p and Mn 2p have two peaks corresponding to the $2p_{3/2}$ and $2p_{1/2}$ sublevels. The core energies of Co and Mn were investigated using curve-fitting models proposed by Biesinger et al. and Nesbitt and Banerjee.[31−33] In $K_{0.5}Mn_{1-x}Co_xO_2$, both Mn and Co can have an oxidation state of +3 or +4. Their chemical states are summarized in Figure 3a. The Mn 2*p* peak deconvolutes into two prominent peaks in the Co-0 and Co-25 samples, and each peak can be further deconvoluted into five peaks. In the case of Co-50 and Co-75, the Mn $2p_{3/2}$ peak at ~642.5 eV can be deconvoluted into five peaks, indicating the presence of Mn solely in the +4 state. In the Co-25 and Co-50 phases, the Co $2p_{3/2}$ peak can be deconvoluted into three peaks with a prominent shoulder, indicating the presence of trivalent cobalt in the compounds. In the Co-75 phase, an additional peak at 781.73 eV clearly establishes the existence of tetravalent cobalt. The valence states of Mn and Co have been presented in different colors in the spectrum: blue peaks indicate 3+, while orange peaks indicate a 4+ chemical state. XPS analysis confirms that the chemical states of Co and Mn in $K_{0.5}Mn_{1-x}Co_xO_2$ compounds are in agreement with their theoretical oxidation state (Table S5). In addition, the O 1*s* spectra show three individual peaks strongly dependent on the composition of the material (Figure S5). The first peak corresponds to the O^{2-} anions in the crystal framework. The second peak may arise due to lattice oxygen with coordination deficiency, while the third peak can be attributed to the surface oxygen. The XPS spectrum of the K 2*p* orbital consists of two distinct peaks, K $2p_{3/2}$ and K $2p_{1/2}$, attributed to the K^+ species. Overall, with higher Co content in $K_{0.5}Mn_{1-x}Co_xO_2$ compounds, Mn tends to oxidize (from +3 to +4) leading to a higher degree of tetravalent Mn in the lattice framework. Co is typically found in 3+ chemical states, with the exception of Co-75, where half of the Co is in the 4+ chemical state.

3.2. Electrochemical Properties. Galvanostatic and potentiodynamic tests were carried out for $K_{0.5}Mn_{1-x}Co_xO_2$ materials in K/K^+ half-cells to evaluate their electrochemical K^+ (de)insertion performance. Cyclic voltammetry was performed on Co-containing cathodes (Co-0, Co-25, Co-50, and Co-75) between 1.5 and 4.0 V at a scan rate of 0.05 mV s^{-1} (Figure 4). The results showed that Co-0 exhibited three oxidation peaks at 2.07 V(O1), 3.18 V(O2), and 3.99 V(O3), with corresponding reduction peaks at 3.34 V(R2) and 2.33 V(R4). In the second cycle, two new peaks appeared during reduction at 3.6 V (R1) and 2.72 V (R3), which were reversible in subsequent cycles. Co-25 displayed four oxidation peaks at 2.12 V(O1), 2.52 V(O2), 3.12 V(O3), and 3.91 V(O4), along with corresponding reduction peaks at 3.35 2.47, 2.05, and 1.63 V (R4). Co-40 samples showed only two redox peaks at lower voltages during the first and subsequent cycles with the peaks at higher voltages absent. Co-50 exhibited oxidation peaks at 2.02 V(O1) and 2.40 V(O2), corresponding reduction peaks at 1.51 V(R2), and 2.0 V(R1), and a small reduction peak at 3.723 V after the first cycle. The Co-60 compound showed well-resolved prominent peaks at higher voltages again. Co-75 showed oxidation peaks at 2.76 V(O1), 3.50 V(O2), and 4.00 V(O3), with corresponding reduction peaks at 2.43 2.95, and 3.68 V(R1), respectively. The consecutive cyclic voltammograms overlapped with each

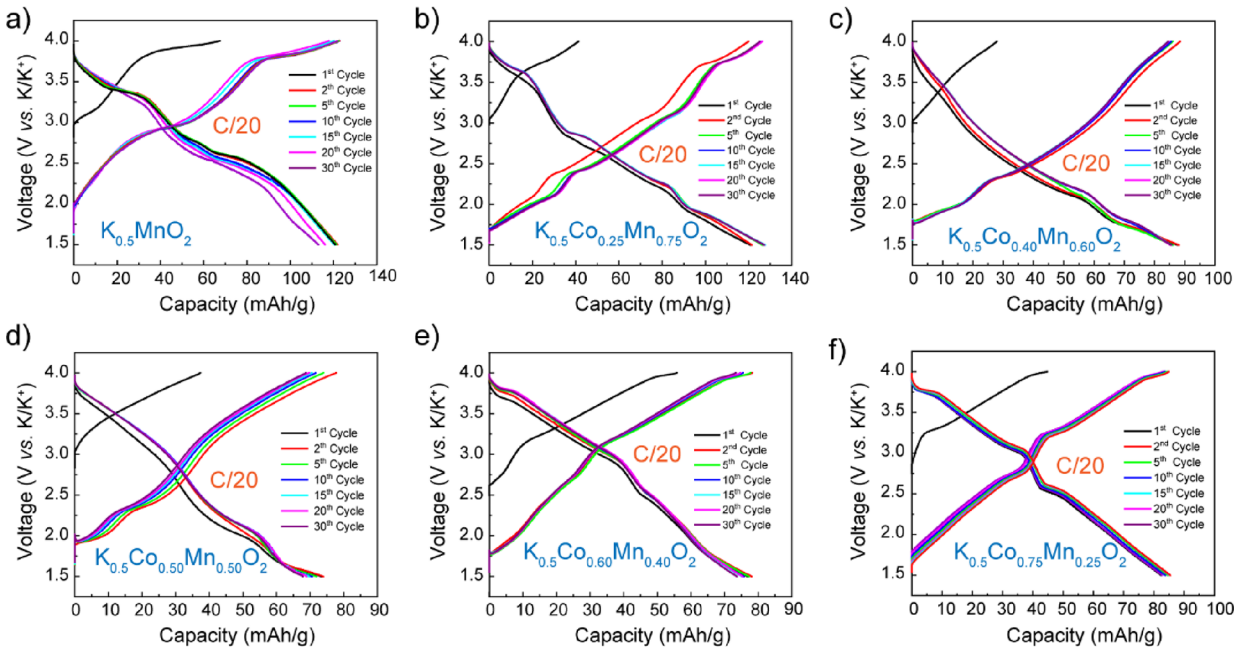

Figure 5. Galvanostatic charge−discharge profiles of P3-type (a) $K_{0.5}MnO_2$, (b) $K_{0.5}Co_{0.25}Mn_{0.75}O_2$, (c) $K_{0.5}Co_{0.40}Mn_{0.60}O_2$, (d) $K_{0.5}Co_{0.5}Mn_{0.5}O_2$, (e) $K_{0.5}Co_{0.60}Mn_{0.40}O_2$, and (f) $K_{0.5}Co_{0.75}Mn_{0.25}O_2$ cathode materials at a specific current of C/20 in the potential window 1.5−4.0 V.

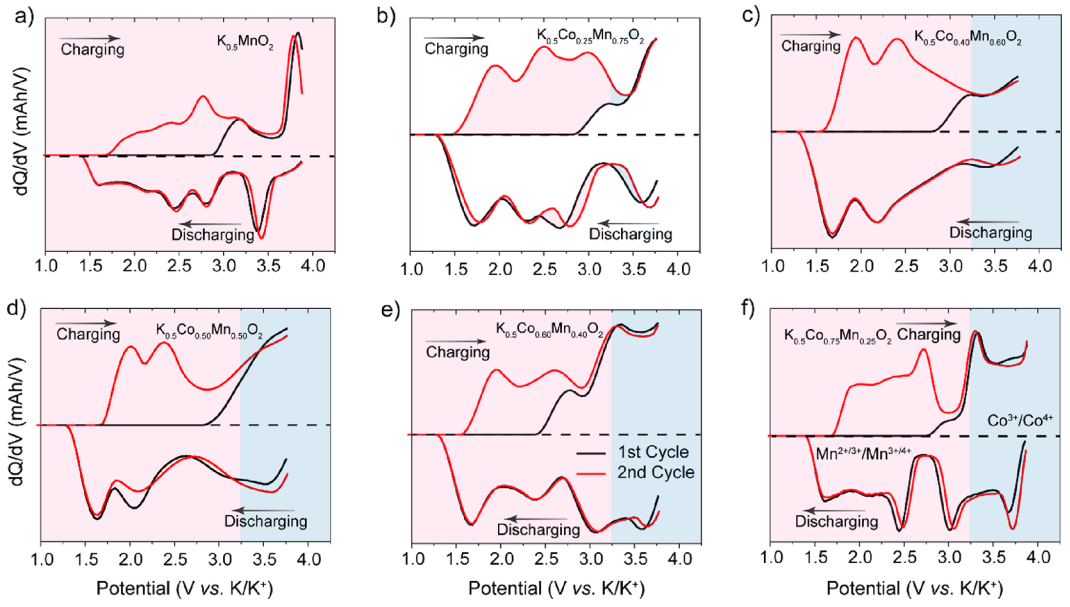

Figure 6. dQ/dV plots for P3-type (a) $K_{0.5}MnO_2$, (b) $K_{0.5}Co_{0.25}Mn_{0.75}O_2$, (c) $K_{0.5}Co_{0.40}Mn_{0.60}O_2$, (d) $K_{0.5}Co_{0.5}Mn_{0.5}O_2$, (e) $K_{0.5}Co_{0.60}Mn_{0.40}O_2$, and (f) $K_{0.5}Co_{0.75}Mn_{0.25}O_2$ vs K/K^+ at the current rate of C/20 in the potential window range of 1.5 to 4.0 V.

other, indicating their high stability and excellent reversibility for K^+ ion (de)insertion. Overall, P3-type $K_{0.5}Mn_{1-x}Co_xO_2$ phases exhibit two redox species: Co and Mn. In the voltage range studied (1.5−4.0 V vs K/K^+), only one redox couple for Co, Co^{3+}/Co^{4+}, was found to be active operating between 3.0 and 4.0 V.

On the other hand, Mn exhibits two redox couples: Mn^{2+}/Mn^{3+} and Mn^{3+}/Mn^{4+}. The Mn^{3+}/Mn^{4+} redox becomes active between 2 and 3.2 V, while the Mn^{2+}/Mn^{3+} couple operates at voltages below 2.0 V and contributes significantly to the overall capacity. The absence of redox peaks at higher voltages for intermediate Co∼50 compounds indicates the absence of Co redox. These findings suggest that both Co and Mn contribute to the electrochemical activity of $K_{0.5}Mn_{1-x}Co_xO_2$, with Mn playing a more significant role at lower voltages. Additionally, minor peaks between 2 and 3 V represented the structural rearrangement of the layers.[17]

Galvanostatic charge−discharge tests were performed on potassium half-cells employing $K_{0.5}Mn_{1-x}Co_xO_2$ materials to evaluate their electrochemical K^+ storage properties. The tests were conducted in the potential range 1.5−4.0 V at a specific current rate of C/20 (Figure 5). As observed in previous reports,[13] the $x = 0$ compound or $K_{0.5}MnO_2$ exhibits a stepwise voltage curve during the (dis)charging process, with multiple potential pseudoplateaus versus K/K^+. It can be ascribed to the complex electronic structure of the material and K^+/vacancy

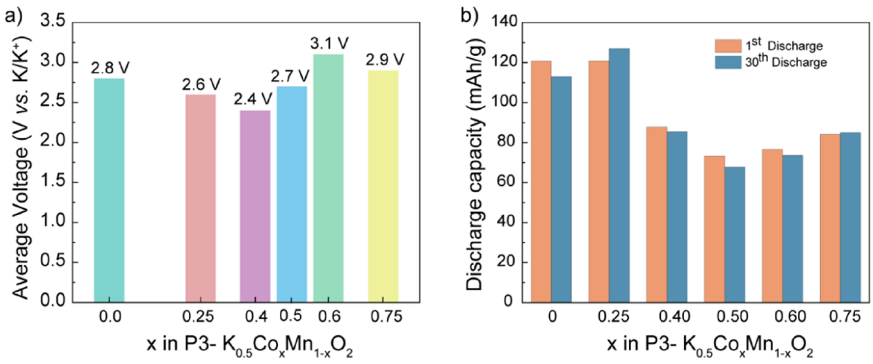

Figure 7. (a) Average voltage and (b) capacity retention plot for P3-type $K_{0.5}Mn_{1-x}Co_xO_2$ (vs K/K^+) at the current rate of C/20 in the potential window range of 1.5 to 4.0 V.

ordering in the layers. The first charge and discharge capacities were 67 and 120 mAh g^{-1}, respectively, suggesting that although ≈0.27 K^+ was removed and ≈0.57 K^+ can be reinserted. However, we observed a reduction in the discharge capacity upon further cycling, implying that the K^+ (de)-insertion processes may cause an irreversible structural change in the high-voltage region. When one-fourth of Mn is substituted by Co, the small plateaus in the charge−discharge profiles disappear and well-defined steps are clearly observed at several potentials. Considerable change was noticed in the charge−discharge profiles upon gradual increment in Co content, where multiple steps disappeared to make the profile smoother. However, at a higher content of Co in the compound, the capacity or the number of K^+ ions (de)-intercalating into the cathode host decays. Only 0.35, 0.30, 0.31, and 0.33 mol of K^+ participate in the redox reaction at x = 0.40, 0.50, 0.60, and 0.75, respectively. The x = 0.75 compound showed a clear multiple symmetric stepwise voltage profile during K^+ (de)insertion, related to the possible K^+/vacancy ordering at different (de)potassiation states. Note that in all cases, a higher specific capacity was achieved during discharge than during the first charge as the first charge process starts at open circuit voltage (OCV) and from the K-deficient phase ($K_{0.5}Mn_{1-x}Co_xO_2$). One may notice that for $x > 0$, the second discharge capacity is slightly higher than the first discharge capacity. In contrast, an increment from 121 to 127 mAh g^{-1} in the second discharge capacity was evident for x = 0.25. With an increase in x ($x > 0.25$), the capacity above 3.0 V corresponding to the Co^{3+}/Co^{4+} redox couple significantly decreased and almost vanished for x = 0.40 and 0.50. In contrast, below 2.5 V, the capacity contribution and voltage profile due to Mn redox remained almost constant, irrespective of composition.

The derivative of the capacity (Q) with respect to the potential (V), dQ/dV, was used to illustrate the influence of Co substitution on the K^+ intercalation process (Figure 6). The plots for the subsequent cycle showed that all of the compositions underwent reversible phase transitions with similar shapes for the anodic and cathodic processes. The presence of two distinct peaks above and many not well-resolved peaks below 2.5 V in $K_{0.5}MnO_2$ indicated the presence of several biphasic states during (de)potassiation.[13] In contrast, all of the peaks were well-defined and well-resolved in the Co-incorporated compounds. It is also noted that the anodic and cathodic peaks in dQ/dV shifted directly with Co content (x). With increasing substitution of Mn by Co, the Co^{3+}/Co^{4+} peaks in the high voltage region shifted to lower voltage.[17] The Mn^{3+}/Mn^{4+} peaks at the low-voltage region shifted toward higher voltage as Co was substituted into the P3-type $K_{0.5}Mn_{1-x}Co_xO_2$. Furthermore, for Co content greater than 0.25, the dQ/dV peak for the Co^{3+}/Co^{4+} redox couple almost vanished for x near 0.5 while retaining the Mn^{3+}/Mn^{4+} redox peaks albeit with a shift in peak position.[17]

Figure 7a plots the average voltage as a function of Co substitution in the P3-$K_{0.5}Mn_{1-x}Co_xO_2$ compounds. In principle, the standard redox potential of Co is higher than the Mn redox potential, and we could expect a linear increase in the average voltage with Co substitution. However, we observed that first the average voltage decreases followed by the observation of the lowest voltage in the case of the Co-40 compound. Beyond Co-40, we observed an increment in the average voltage with a higher Co content in the host framework. The absence of the Co^{3+}/Co^{4+} redox in the Co-40 sample could be the reason for the lowest average voltage.[17] This anomalous trend in the average redox potential is complex. We postulate that the inductive effects of Mn and Co on each other can significantly impact the redox chemistry of their respective ions. The inductive effect of manganese (Mn) on the cobalt−oxygen (Co−O) bonding can result in the hybridization of Mn t_{2g} orbitals into the Co-0 t_{2g} (π) band. This can cause a lowering of the chemical potential of the Co^{3+}/Co^{4+} redox couple due to the increased electron density in the Co−O bond.[17] On the other hand, the inductive effect of cobalt (Co) on the manganese−oxygen (Mn−O) bonding can lead to an increase in the chemical potential of the Mn^{3+}/Mn^{4+} redox couple.[17] This is because the Co atoms pull the electron density away from the Mn−O bond, making it more challenging to remove an electron from the Mn atom and thus increasing the energy required to oxidize Mn^{3+} to Mn^{4+}.

Furthermore, Figure 7b summarizes the specific discharge capacity at the 1st and 30th cycles during the redox processes for P3-$K_{0.5}Mn_{1-x}Co_xO_2$. As Co replaces Mn, we observed a reduction in the first discharge capacity for all materials. Additionally, the cycling stability for high Mn compound improves with Co substitution. The replacement of Co with Mn in P3-type $K_{0.5}Mn_{1-x}Co_xO_2$ may impede the formation of the passivating layer at the electrode surface to improve the cyclability of the electrode.[17,34] Notably, the second discharge capacity is greater than the first discharge capacity for all of the phases. Charge−discharge curves are smooth and symmetric for the higher Co-containing compounds devoid of multiple unresolved and asymmetric plateaus. Importantly, ex situ X-ray diffraction analyses were conducted for samples with both low ($K_{0.5}Co_{0.25}Mn_{0.75}O_2$) and high ($K_{0.5}Co_{0.75}Mn_{0.25}O_2$) Co

content to investigate the K^+ storage mechanism. The XRD patterns at fully (dis)charged states distinctly confirmed the integrity of the P3 phase without the appearance of any additional peaks along with steady peak shift implying a single phase K^+ (de)intercalation process (Figure S6). In congruence, ex situ XPS of $K_{0.5}Co_{0.25}Mn_{0.75}O_2$ at different s tates of (dis)charge revealed the presence of Mn^{3+}/Mn^{2+} redox activity below 2 V (Figure S7). Finally, we propose Co-rich composition with all Mn in the 4+ oxidation state can provide structural stability for the optimal electrochemical performance in KIBs. It is necessary to optimize and explore the interface for a better fundamental understanding of polarization, capacity loss, and structural integrity during (de)potassiation.

4. CONCLUSIONS

In this work , we have investigated the P3-$K_{0.5}Mn_{1-x}Co_xO_2$ family as a cathode intercalation host material for secondary K-ion batteries. We have also elucidated the effect of Co addition on electrochemical properties and structural integrity. The structural stability and capacity retention improved with increasing Co substitution, while the discharge capacity exhibited an initial increase followed by a significant reduction at intermediate concentrations of Co. The improved capacity retention is due to the enhanced structural stability, which is attributed to the suppression of the Jahn−Teller distortion. The results demonstrated that substituting Co significantly impacted the K^+ intercalation process in P3-$K_{0.5}Mn_{1-x}Co_xO_2$ oxides. Due to the inductive effect of transition metals on each other, with the substitution of Co in the material, the redox potential of Co^{3+}/Co^{4+} shifted to a lower potential while the redox potential of Mn^{3+}/Mn^{4+} moved to a higher potential. All $K_{0.5}Mn_{1-x}Co_xO_2$ phases had similar Mn^{3+}/Mn^{4+} redox peaks. These findings s uggest t hat t he e lectrochemical p roperties of the P3-type $K_{0.5}Mn_{1-x}Co_xO_2$ cathodes for potassium-ion batteries can be enhanced by partial Co substitution. This study offers a s tep f orward i n o ptimizing t he electrochemical performance of layered oxide cathode materials for rechargeable K-ion batteries.

AUTHOR INFORMATION

Corresponding Author

Prabeer Barpanda − *Faraday Materials Laboratory (FaMaL), Materials Research Centre, Indian Institute of Science, Bangalore 560012, India; Helmholtz Institute Ulm (HIU), Electrochemical Energy Storage, Ulm 89081, Germany; Institute of Nanotechnology, Karlsruhe Institute of Technology (KIT), Karlsruhe 76021, Germany;* orcid.org/0000-0003-0902-3690; Email: prabeer@iisc.ac.in; Fax: + 91 80 2360 7316

Author

Pawan Kumar Jha − *Faraday Materials Laboratory (FaMaL), Materials Research Centre, Indian Institute of Science, Bangalore 560012, India*

Author Contributions

P.K.J.: conceptualization, data curation, formal analysis, investigation, methodology, writing—original draft; P.B.: conceptualization, funding acquisition, formal analysis, project administration, supervision, writing—review and editing.

Notes

The authors declare no competing financial interest.

■ ACKNOWLEDGMENTS

The current work was financially supported by the Core Research Grant (Science and Engineering Research Board, SERB, Govt. of India) (CRG/2022/000963). The first author is grateful to the Ministry of Human Resource Development (MHRD, Government of India) for a graduate fellowship. He also thanks Prof. S. G. Gopalakrishnan for scientific discussions. P.B. thanks Prof. M. Fichtner for technical discussion and the Alexander von Humboldt Foundation (Bonn, Germany) for a 2022 Humboldt fellowship for experienced researchers.

■ REFERENCES

(1) Dunn, B.; Kamath, H.; Tarascon, J.-M. Electrical Energy Storage for the Grid: A Battery of Choices. *Science* **2011**, *334*, 928−935.

(2) Whittingham, M. S. Ultimate Limits to Intercalation Reactions for Lithium Batteries. *Chem. Rev.* **2014**, *114*, 11414−11443.

(3) Hosaka, T.; Kubota, K.; Hameed, A. S.; Komaba, S. Research Development on K-Ion Batteries. *Chem. Rev.* **2020**, *120*, 6358−6466.

(4) Kim, H.; Kim, J. C.; Bianchini, M.; Seo, D.-H.; Rodriguez-Garcia, J.; Ceder, G. Recent Progress and Perspective in Electrode Materials for K-Ion Batteries. *Adv. Energy Mater.* **2018**, *8*, No. 1702384.

(5) Okoshi, M.; Yamada, Y.; Komaba, S.; Yamada, A.; Nakai, H. Theoretical Analysis of Interactions between Potassium Ions and Organic Electrolyte Solvents: A Comparison with Lithium, Sodium, and Magnesium Ions. *J. Electrochem. Soc.* **2017**, *164*, A54.

(6) Jha, P. K.; Pralong, V.; Fichtner, M.; Barpanda, P. P3 type layered oxide frameworks: An appealing family of insertion materials for K-ion batteries. *Curr. Opin. Electrochem.* **2023**, *38*, No. 101216.

(7) Kim, H.; Ji, H.; Wang, J.; Ceder, G. Next-Generation Cathode Materials for Non-aqueous Potassium-Ion Batteries. *Trends Chem.* **2019**, *1*, 682−692.

(8) Zhang, X.; Wei, Z.; Dinh, K. N.; Chen, N.; Chen, G.; Du, F.; Yan, Q. Layered Oxide Cathode for Potassium-Ion Battery: Recent Progress and Prospective. *Small* **2020**, *16*, No. 2002700.

(9) Fouassier, C.; Delmas, C.; Hagenmuller, P. Evolution Structurale et Proprietes Physiques des Phases A_XMO_2 (A = Na, K; M = Cr, Mn, Co) ($x \leqslant 1$). *Mater. Res. Bull.* **1975**, *10*, 443−449.

(10) Zhao, C.; Wang, Q.; Yao, Z.; Wang, J.; Sánchez-Lengeling, B.; Ding, F.; Qi, X.; Lu, Y.; Bai, X.; Li, B.; Li, H.; Aspuru-Guzik, A.; Huang, X.; Delmas, C.; Wagemaker, M.; Chen, L.; Hu, Y.-S. Rational Design of Layered Oxide Materials for Sodium-ion Batteries. *Science* **2020**, *370*, 708−711.

(11) Delmas, C.; Fouassier, C.; Hagenmuller, P. Structural Classification and Properties of the Layered Oxides. *Phys. B+C* **1980**, *99*, 81−85.

(12) Delmas, C.; Fouassier, C. Les Phases K_xMnO_2 ($x \leq 1$). *Z. Anorg. Allg. Chem.* **1976**, *420*, 184−192.
(13) Kim, H.; Seo, D.-H.; Kim, J. C.; Bo, S.-H.; Liu, L.; Shi, T.; Ceder, G. Investigation of Potassium Storage in Layered P3-Type $K_{0.5}MnO_2$ Cathode. *Adv. Mater.* **2017**, *29*, No. 1702480.
(14) Yabuuchi, N.; Kubota, K.; Dahbi, M.; Komaba, S. Research Development on Sodium-Ion Batteries. *Chem. Rev.* **2014**, *114*, 11636−11682.
(15) Wang, Q.-C.; Hu, E.; Pan, Y.; Xiao, N.; Hong, F.; Fu, Z.-W.; Wu, X.-J.; Bak, S.-M.; Yang, X.-Q.; Zhou, Y.-N. Utilizing Co^{2+}/Co^{3+} Redox Couple in P2-Layered $Na_{0.66}Co_{0.22}Mn_{0.44}Ti_{0.34}O_2$ Cathode for Sodium-Ion Batteries. *Adv. Sci.* **2017**, *4*, No. 1700219.
(16) Zhang, Q.; Didier, C.; Pang, W. K.; Liu, Y.; Wang, Z.; Li, S.; Peterson, V. K.; Mao, J.; Guo, Z. Structural Insight into Layer Gliding and Lattice Distortion in Layered Manganese Oxide Electrodes for Potassium-Ion Batteries. *Adv. Energy Mater.* **2019**, *9*, No. 1900568.
(17) Wang, X.; Tamaru, M.; Okubo, M.; Yamada, A. Electrode Properties of P2−$Na_{2/3}Mn_yCo_{1-y}O_2$ as Cathode Materials for Sodium-Ion Batteries. *J. Phys. Chem. C* **2013**, *117*, 15545−15551.
(18) Choi, J. U.; Kim, J.; Hwang, J.-Y.; Jo, J. H.; Sun, Y.-K.; Myung, S.-T. $K_{0.54}[Co_{0.5}Mn_{0.5}]O_2$: New Cathode with High Power Capability for Potassium-ion Batteries. *Nano Energy* **2019**, *61*, 284−294.
(19) Ramasamy, H. V.; Senthilkumar, B.; Barpanda, P.; Lee, Y.-S. Superior Potassium-ion Hybrid Capacitor Based on Novel P3-type Layered $K_{0.45}Mn_{0.5}Co_{0.5}O_2$ as High Capacity Cathode. *Chem. Eng. J.* **2019**, *368*, 235−243.
(20) Sada, K.; Barpanda, P. P3-type layered $K_{0.48}Mn_{0.4}Co_{0.6}O_2$: A Novel Cathode Material for Potassium-ion Batteries. *Chem. Commun.* **2020**, *56*, 2272−2275.
(21) Rodríguez-Carvajal, J. Recent Advances in Magnetic Structure Determination by Neutron Powder Diffraction. *Physica B: Condensed Matter* **1993**, *192*, 55−69.
(22) Momma, K.; Izumi, F. VESTA 3 for Three-dimensional Visualization of Crystal, Volumetric and Morphology Data. *J. Appl. Cryst.* **2011**, *44*, 1272−1276.
(23) Yoshii, K.; Masese, T.; Kato, M.; Kubota, K.; Senoh, H.; Shikano, M. Sulfonylamide-Based Ionic Liquids for High-Voltage Potassium-Ion Batteries with Honeycomb Layered Cathode Oxides. *ChemElectroChem.* **2019**, *6*, 3901−3910.
(24) Shannon, R. Revised Effective Ionic Radii and Systematic Studies of Interatomic Distances in Halides and Chalcogenides. *Acta Crystallogr.* **1976**, *32*, 751−767.
(25) Khatun, F.; Gafur, M. A.; Ali, M. S.; Islam, M. S.; Sarker, M. A. R. Impact of Lithium Composition on Structural, Electronic and Optical Properties of Lithium Cobaltite Prepared by Solid-state Reaction. *J. Sci. Res.* **2014**, *6*, 217−231.
(26) Duncan, H.; Hai, B.; Leskes, M.; Grey, C. P.; Chen, G. Relationships between Mn^{3+} Content, Structural Ordering, Phase Transformation, and Kinetic Properties in $LiNi_xMn_{2-x}O_4$ Cathode Materials. *Chem. Mater.* **2014**, *26*, 5374−5382.
(27) Paulsen, J. M.; Dahn, J. R. Studies of the Layered Manganese Bronzes, $Na_{2/3}[Mn_{1-x}M_x]O_2$ with M = Co, Ni, Li, and $Li_{2/3}[Mn_{1-x}M_x]O_2$ Prepared by Ion-exchange. *Solid State Ion.* **1999**, *126*, 3−24.
(28) Jia, S.; Yao, E.; Peng, R.; Jonderian, A.; Abdolhosseini, M.; McCalla, E. Chemical Speed Dating: The Impact of 52 Dopants in Na−Mn−O Cathodes. *Chem. Mater.* **2022**, *34*, 11047−11061.
(29) Baddour-Hadjean, R.; Pereira-Ramos, J.-P. Raman Microspectrometry Applied to the Study of Electrode Materials for Lithium Batteries. *Chem. Rev.* **2010**, *110*, 1278−1319.
(30) Inaba, M.; Yoshida, H.; Ogumi, Z.; Abe, T.; Mizutani, Y.; Asano, M. In Situ Raman Study on Electrochemical Li Intercalation into Graphite. *J. Electrochem. Soc.* **1995**, *142*, 20.
(31) Hemalatha, K.; Jayakumar, M.; Prakash, A. S. Influence of the Manganese and Cobalt Content on the Electrochemical Performance of P2-$Na_{0.67}Mn_xCo_{1-x}O_2$ Cathodes for Sodium-ion Batteries. *Dalton Trans.* **2018**, *47*, 1223−1232.
(32) Biesinger, M. C.; Payne, B. P.; Grosvenor, A. P.; Lau, L. W. M.; Gerson, A. R.; Smart, R. S. C. Resolving Surface Chemical States in XPS Analysis of First Row Transition Metals, Oxides and Hydroxides: Cr, Mn, Fe. *Co and Ni. Appl. Surf. Sci.* **2011**, *257*, 2717−2730.
(33) Nesbitt, H. W.; Banerjee, D. Interpretation of XPS Mn(2*p*) spectra of Mn Oxyhydroxides and Constraints on the Mechanism of MnO_2 Precipitation. *Am. Mineral.* **1998**, *83*, 305−315.
(34) Clément, R. J.; Bruce, P. G.; Grey, C. P. Review—Manganese-Based P2-Type Transition Metal Oxides as Sodium-Ion Battery Cathode Materials. *J. Electrochem. Soc.* **2015**, *162*, A2589.